

Identification of a Potential Thiazole Inhibitor Against Biofilms by 3D QSAR, Molecular Docking, DFT Analysis, MM-PBSA Binding Energy Calculations, and Molecular Dynamics Simulation

K. Tabti^a, H. Hajji^a, A. Sbai^{a,*}, H. Maghat^a, M. Bouachrine^{a,b} and T. Iakhlifi^a

^aMolecular Chemistry and Natural Substances Laboratory, Moulay Ismail University, Faculty of Science, Meknes, Morocco

^bHigher School of Technology-EST Khenifra, Sultan Moulay Sliman University, Benimellal, Morocco

(Received 31 March 2022, Accepted 6 July 2022)

In this study, computational approaches were invested on a thiazole derivatives as biofilm inhibitor agents. CoMFA and CoMSIA models constructed presented a significant predictive capacity, including Q^2 values of 0.538 and 0.593 and R^2 values of 0.925 and 0.905 and R^2_{pred} values of 0.867 and 0.913, and ESS values of 0.185 and 0.208, respectively. The predictability check was performed by external validation, which shows that the CoMSIA model strongly explains the inhibitory activity against biofilms. The information generated by the CoMSIA model has guided us to propose some candidates as a potent biofilm inhibitor. The mode of interaction was examined by molecular docking on a protein-binding pocket (ID: 2XF). The results obtained highlight the key amino acids involved in the ligand/protein interaction and show that the complexes bound to the designed compounds showed the best conformations in the binding site. An ADMET study was carried out on the various compounds proposed to ensure their pharmacokinetics and bioavailability in the body. The binding stability of the most active compound N°22, the lowest active compound N°8, and the newly designed compound Pred01 was assessed by molecular dynamics simulations accompanied by the calculation of the binding free energy according to a simulation trajectory of 100 ns. Furthermore, the energy profiles of these selected compounds were described by DFT analysis. Finally, these findings could lead to the discovery of new, more effective thiazole-based antibiofilm inhibitors.

Keywords: Biofilm, Thiazole, 3D-QSAR, Docking molecular, DFT, MD Simulations

INTRODUCTION

According to the National Institutes of Health (NIH), Biofilms contribute 65-80% of the total microbiological infections and 80-90% of chronic infections [1-3]. In addition, statistics indicate that drug-resistant diseases kill approximately 25,000 life in Europe and 23,000 lives in the United States annually, with the proportion significantly higher in developing countries [4,5]. These statistics make biofilm a serious health problem for the world.

The bacterial biofilms are known to be complex structured aggregates of microbes on an inert or living

surface such as body surfaces, medical devices, and plants [6-8]. Microorganisms that grow in a biofilm resist adaptively antibiotics stronger than the same bacteria due to numerous phenotypic mechanisms. Where, bacterial cells in a biofilm are covered by the matrix, which prevents antibiotics from penetrating, and the deeper layers bear metabolic inactivation, resulting in the creation of persistent inactive cells that are naturally difficult to treat [9,10]. Hence, the formation of microbial biofilms is among the main reasons for the failure of antibiotic therapy [11,12]. The effect of biofilm formation on drug resistance highlights the importance of developing novel inhibitory agents capable of preventing biofilm formation and thus avoiding drug-resistant infections [13], especially with recent events such as COVID-19 [14], where antibiotics have become overused

*Corresponding author. E-mail: a.sbai@umi.ac.ma

and thus an increase in Antibiotic resistance. Despite numerous efforts in recent years to finding of several compounds as antibiofilm agents, no compound has been approved for clinical use at present [15].

This current research was devoted to establishing a quantitative structure-activity relationship (QSAR) of thiazole derivative compounds as biofilm inhibitors, in order to further establish new biofilm inhibitor compounds based on thiazole derivatives. Although QSAR develops models for the prediction of new potent compounds [16,17]. The companionship of 3D QSAR by molecular docking methods and molecular dynamics simulations is the most powerful and recognized approach to design new powerful compounds in the field of computer-aided drug design [18]. On the one hand, the molecular docking technique estimates the binding mode and mechanism of a ligand in the target active site of a protein [19,20]. On the other hand, the molecular dynamics simulations guides to evaluate the ligand stability in the binding site, and also to estimate the binding free energy using the MM-PBSA approach [21,22]. The model developed led us to develop eleven compounds with higher inhibitory activity than the most active molecule in the data set compound N°22. Our work was reinforced by an ADME/toxicity study to predict the bioavailability of these proposed compounds compared to compound N°22. The energy profile of the compounds and their reactivity was studied using the DFT study. Finally, all these results can build a solid and interesting path for the design of new biofilm inhibitors.

MATERIALS AND RESEARCH METHOD

Dataset Preparation

In this research, a dataset including 27 thiazole-derived compounds as antibiofilm agents against bacterial reference strains *S. aureus* (ATCC 25923) was collected for the generation of 3D-QSAR models [23]. The inhibitory concentration IC_{50} was transformed into pIC_{50} ($-\log IC_{50}$) for use as a dependent variable, the recorded IC_{50} values of the dataset vary between 4.312 M and 6.699 M. Four molecules (15%) from the datasets were randomly selected as a test set to assess the predictive ability of the constructed models, and the rest of the molecules (23 molecules, 85%) were considered as a training set to generate 3D-QSAR models.

The structure of all selected compounds and their reported activity values (pIC_{50}) are listed in Table 1.

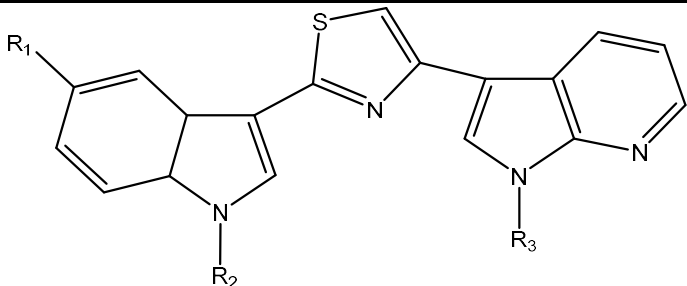
Dataset preparation and alignment procedure. The structures of all targeted compounds in the dataset were drawn using SYBYL-X 2.0 software. A Tripos force field with 0.05 kcal/(mol/Å) and Powell's conjugate minimization algorithm with 1000 iterations were used as parameters to energetically minimize the geometry of all structures of thiazole derivatives [24]. The partial atomic charge was calculated by the method of Gasteiger Huckel, then it was added to the molecules to obtain stable molecular conformations [23,24]. The other program parameters SYBYL-X 2.0 have been adopted by default. The molecular alignment of the compounds was carried out by the method of distilling rigid alignment implanted in SYBYL-2.0, as is shown in Fig. 1. The most activity molecule N°22 was chosen as a template.

Molecular modeling by CoMFA and CoMSIA analysis. SYBYL-X 2.0 software was used to develop 3D-QSAR models based on selected thiazole derivatives using the two most widely used methods, CoMFA and CoMSIA. CoMFA makes it possible to correlate the biological activity with the steric (S) and electrostatic (E) properties. The steric and electrostatic fields were estimated on a 3D grid with a spacing of 2.0 Å in three spatial directions for each of the alignments [25]. To count the energy of steric fields, an sp^3 carbon probe atom with a Lennard-Jones Coulomb radius of 1.52 Å was taken and the electrostatic energy was calculated with a charge of +1 as probe [26]. The cutoff value for steric and electrostatic fields was maintained at 30.0 kcal mol⁻¹. The Lennard-Jones (1) and Coulomb (2) relations are calculated according to the following:

$$E_{vdw} = \sum_{i=1}^n (A_i r_{ij}^{-12} - C_j r_{ij}^{-6}) \quad (1)$$

$$E_C = \sum_{i=1}^n q_i q_j / D r_{ij} \quad (2)$$

In the case of the CoMSIA method, it makes it possible to correlate the biological activity with the steric (S) and electrostatic (E), hydrophobic (H), hydrogen bond acceptor (A), and hydrogen bond donor (D) properties. The similarity is represented in terms of steric and electrostatic properties, the values of the other standard parameters at the probe

Table 1. Chemical Structures and Inhibitory Activities of the Compounds Studied


The chemical structure shows a thiazole ring connected to a benzimidazole system. The thiazole ring has a sulfur atom at the top and a nitrogen atom at the bottom. It is connected to a benzimidazole system at the 2-position. The benzimidazole system consists of a benzene ring fused to an imidazole ring. The nitrogen atom of the imidazole ring is substituted with R₃. The benzene ring of the benzimidazole system has a substituent R₁ at the 6-position. The nitrogen atom of the benzimidazole system is substituted with R₂.

N°		R ₁	R ₂	R ₃	pIC ₅₀ exper (M)	CoMFA pIC ₅₀ pred	Res	CoMSIA pIC ₅₀ pred	Res	Affinity (kcal mol ⁻¹)
1	Train	H	CH ₂ CH ₂ NHBoc	CH ₃	4.86	4.908	-0.048	4.865	-0.005	-7.9
2	Train	OCH ₃	CH ₂ CH ₂ NHBoc	H	5.149	5.101	0.048	5.083	0.066	-8.1
3	Train	Br	CH ₂ CH ₂ NHBoc	CH ₃	5.032	4.74	0.292	4.768	0.264	-8.1
4	Train	F	CH ₂ CH ₂ NHBoc	CH ₃	4.433	4.673	-0.24	4.707	-0.274	-8.1
5	Train	H	CH ₂ CH ₂ NH ₂	H	5.328	5.362	-0.034	5.399	-0.071	-7.8
6	Train	H	CH ₂ CH ₂ NH ₂	CH ₃	4.483	4.557	-0.074	4.523	-0.04	-7.2
7	Train	OCH ₃	CH ₂ CH ₂ NH ₂	H	4.633	4.358	0.275	4.451	0.182	-7.6
8	Train	OCH ₃	CH ₂ CH ₂ NH ₂	CH ₃	4.312	4.609	-0.297	4.635	-0.323	-7.3
9	Train	Br	CH ₂ CH ₂ NH ₂	H	5.357	5.654	-0.297	5.696	-0.339	-7.9
10	Train	Br	CH ₂ CH ₂ NH ₂	CH ₃	4.697	4.661	0.036	4.62	0.077	-7.2
11	Train	F	CH ₂ CH ₂ NH ₂	H	5.824	5.894	-0.07	5.873	-0.049	-7.8
12	Train	F	CH ₂ CH ₂ NH ₂	CH ₃	6.301	5.947	0.354	5.839	0.462	-7.2
13	Train	H	CH ₃	CH ₂ CH ₂ Ome	5.125	5.15	-0.025	5.163	-0.038	-7.2
14	Test	OCH ₃	CH ₂ CH ₂ Ome	H	4.73	5.648	-0.918	6.13	-1.4	-7.4
15	Train	OCH ₃	CH ₂ CH ₂ Ome	CH ₃	5.921	5.979	-0.058	5.974	-0.053	-7.4
16	Train	OCH ₃	CH ₂ CH ₂ Ome	CH ₂ CH ₂ Ome	5.102	5.065	0.037	5.059	0.043	-6.7
17	Train	Br	CH ₂ CH ₂ Ome	H	6.102	6.002	0.1	5.957	0.145	-7.9
18	Train	Br	CH ₂ CH ₂ Ome	CH ₃	6.022	6.098	-0.076	6.072	-0.05	-7.3
19	Train	Br	CH ₂ CH ₂ Ome	CH ₂ CH ₂ Ome	5.538	5.516	0.022	5.652	-0.114	-6.6
20	Train	Br	CH ₃	CH ₂ CH ₂ Ome	5.602	5.593	0.009	5.606	-0.004	-7.0
21	Test	F	CH ₂ CH ₂ Ome	CH	4.86	5.931	-1.071	6.256	-1.396	-7.9
22	Test	F	CH ₂ CH ₂ Ome	CH ₃	6.699	4.716	1.983	5.131	1.568	-7.3
23	Train	F	CH ₂ CH ₂ Ome	CH ₂ CH ₂ Ome	4.545	4.539	0.006	4.444	0.101	-6.9
24	Train	F	H	CH ₂ CH ₂ Ome	4.863	4.853	0.01	4.922	-0.059	-7.8
25	Test	H	Boc	CH ₂ CH ₂ Ome	5.745	4.954	0.791	5.377	0.368	-7.4
26	Train	H	H	CH ₂ CH ₂ Ome	4.889	4.824	0.065	4.81	0.079	-7.8
27	Train	Br	H	CH ₂ CH ₂ Ome	4.883	4.917	-0.034	4.882	0.001	-7.7

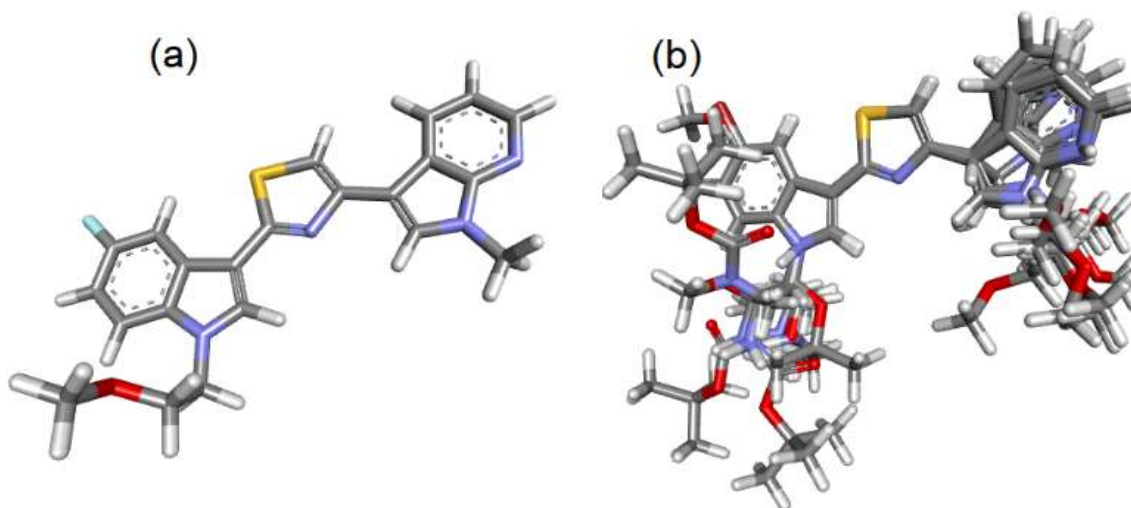


Fig. 1. Superposition structure aligned of the 27 studied compounds using compound N°22 as a template.

with charge +1, radius 1 Å, +1.0 for the hydrophobic descriptor fields, hydrogen bond donor and acceptor respectively [27,28]. The value of attenuation factor is set by default to 0.3 [29]. The CoMSIA analysis determines the similarity descriptors by means of a lattice grid. For a compound *j* with atoms *I* at the grid point *q*, the CoMSIA AF similarity index is determined by the following formula (3):

$$A_{F,K}^q = - \sum_{i=1}^n w_{probe,k} w_{ik} e^{-ar_{iq}^2} \quad (3)$$

Where w_{ik} is the real value of the physico-chemical property *k* of atom *I*; $w_{probe,k}$ expresses the property of the probe atom with a predefined charge at +1, r_{iq} is the mutual distance between atom *I* of the compound and the probe atom at the grid point *q*.

PLS method. The PLS analysis method is one of the most popular methods to establish relationships explaining the pIC_{50} bioactivity as a dependent variable according to the CoMFA and CoMSIA fields as independent variables [30,31]. PLS is a regression extension that applies a linear transformation of the descriptor space to detect new variables that are linear combinations of the original variables. The calculation of Q^2 and the optimal number of components (ONC) were performed by cross-validation (LOO) where the value of ONC was determined for the lower value of Q^2 . The coefficient of cross validation Q^2 was calculated according to the following formulas (4):

$$Q^2 = 1 - \frac{\sum(y_i - y'_i)^2}{\sum(y_i - y_{mean})^2} \quad (4)$$

In addition, the statistical value of Fischer (F) and the standard error of estimate (SEE) were determined to further assess the stability of the established models. Generally, a high Q^2 coefficient value in the training set implies a good internal validation, but this did not indicate the good predictive ability of the generated 3D-QSAR models, therefore to fill this gap, external validation was performed. In order to assess the predictive power of the models, the predictive correlation coefficient R^2_{pred} was estimated using the test set, using the formula[32]:

$$R^2_{pred} = (SD - PRESS)/SD \quad (5)$$

To ensure better performance of the generated models, other statistical parameters were evaluated by following Eqs. (6)-(13):

$$r_0^2 = 1 - \frac{\sum(y_i - k \times \hat{y}_i)^2}{\sum(y_i - \bar{y}_i)^2} \quad (6)$$

$$(r^2 - r_0^2)/r^2 < 0.1 \quad (7)$$

$$r'^2_0 = 1 - \frac{\sum(\hat{y}_i - k' \times y_i)^2}{\sum(\hat{y}_i - \bar{y})^2} \quad (8)$$

$$(r^2 - r_0'^2) / r^2 < 0.1 \quad (9)$$

$$k = \frac{\sum(y_i - \hat{y}_i)}{(\hat{y}_i)^2} \quad (10)$$

$$r_m^2 = r^2(1 + \sqrt{r^2 - r_0'^2}) \quad (11)$$

$$k = \frac{\sum(y_i - \hat{y}_i)}{(y_i)^2} \quad (12)$$

$$\Delta r_m^2 = |r_m^2 - r_0'^2| \quad (13)$$

Where k and k' are the slope of the predicted (y) values to those observed (\hat{y}) for the test set with zero intercepts and vice versa respectively, $0.85 < k < 1.15$; $0.85 < k' < 1.15$.

Docking Molecular Analysis

AutoDock 1.5.6 software was used to operate the docking analysis. The docking protocol began with the preparation of the protein structure by extracting the co-crystallized reference ligand (PG4) and water molecules from the crystal structure [33]. Polar hydrogen atoms have been added, and the protein chain has been charged with Gasteiger charges. To prevent unnecessary conformational explosions, the number of rotary links was considered. The co-crystallized ligand was positioned in the centre of the grille, and then the grille parameters were generally assumed utilizing AutoGrid program, with the size set to $24 \times 24 \times 24$ points and the spacing set to 0.75 \AA . All through docking, the protein was maintained in a rigid state while the ligand was allowed to be incredibly flexible. Validation of the docking protocol adopted by estimating the value of RMSD between the pose of the referential co-crystallized ligand and the redocked co-crystallized.

MD Simulations and Calculate Binding Free Energy

In order to run an MDsimulations for 100 ns, the GROMACS 2018 software package with 3OPLS as the force field was applied. The systems selected for MD were immersed in a single water model SPC in a cubic box [34]. To simulate physiological conditions, the system was

neutralized by adding 0.15 M Na^+ and Cl^- . The entire system was subjected to 50.000 energy minimization steps using the steepest descent integrator to release the internal strain energies of the entire system. Subsequently, NVT and NPT equilibration was carried out for 0.1 ns at 300 K and 1 bar of pressure. The Berendsen thermostat [35] and the Parrinello-Rahman barostat were used to regulate the temperature and pressure of the system [36]. Long-distance Coulomb interactions have been regulated using the Ewald (PME) particle mesh technique [37].

The binding free energies (ΔG_{Bind}) of the screened complexes were estimated from molecular mechanics of the Poisson-Boltzmann surface (MM-PBSA) using the `g_mmpbsa` package [38,39]. The MM-PBSA approach is one of the most widely used methods for calculating ligand/protein interaction energies. In general, the free energy of binding (G_{Bind}) of a complex in a solvent can be evaluated as follows:

$$\Delta G_{\text{Bind}} = G_{\text{Complex}} - (G_{\text{Protein}} + G_{\text{Ligand}}) \quad (14)$$

where

The term " G_{Complex} " refers to the protein-ligand complex's total free energy, and G_{Protein} and G_{Ligand} are the total free energies of the protein and the ligand when they are separated from the solvent.

Density Functional Theory Studies (DFT)

This manuscript also presents a computational DFT study. Optimization of molecules was carried out with the basis set 6-311G of the Gaussian program and Gauss View for the visualizations [40], this base set is considered more powerful for organic compounds since it shows interesting results of electronic and geometric properties [41]. DFT is a quantum chemistry method, that was applied to investigate in detail the structural aspects and energy states of each ligand atom. To achieve this goal, the energy of highest occupied molecular orbital (E_{HOMO}), energy of lowest unoccupied molecular orbital (E_{LUMO}) and molecular electrostatic potential (MESP) were calculated using B3LYP (Lee-Yang-Parr correlation functional theory). Other quantitative chemical parameters were derived from E_{HOMO} and E_{LUMO} were calculated according to the following formulas (15)-(23).

$$\text{Ionization Potential (IP)} = -E_{HOMO} \quad (15)$$

$$\text{Chemical Softness (S)} = 1/\eta \quad (16)$$

$$\text{Electron Affinity (EA)} = -E_{LUMO} \quad (17)$$

$$\text{Electrophilicity Index}(\omega) = \mu^2/2\eta \quad (18)$$

$$\text{Electronegativity}(\chi) = (IP + EA)/2 \quad (19)$$

$$\text{Energy Change}(\Delta E) = -\mu^2/2\eta \quad (20)$$

$$\text{Chemical Potential}(\mu) = -\chi \quad (21)$$

$$\text{Maximal Charge Acceptance}(\Delta N_{max}) = \mu/\eta \quad (22)$$

$$\text{Chemical Hardness}(\eta) = (IP - EA)/2 \quad (23)$$

ADME/Toxicity Analysis

The compound is a good drug candidate if it verifies the ADME/toxicity properties (absorption, distribution, metabolism, excretion, and toxicity), but the problem is that if the determination of these properties *in vitro* takes the enormous cost and time [42]. In the present work, *in silico*, ADME/toxicity was calculated using the online server pkCSM (<http://bleoberis.bioc.cam.ac.uk/pkcsml/>) [43,44].

RESULTS AND ANALYSIS

Statistical 3D-QSAR Results

In this study, we have generated a CoMFA and 31 CoMSIA models with different possible combinations of steric (S), electrostatic (E), hydrophobic (H), and hydrogen binding donor/acceptor (D/A) fields (Fig. 2). The dependence

on the five descriptors of CoMSIA could decrease the significance of the model [45]. Figure 2 represents the result of all models generated with values of Q^2 and R^2 . Twelve models showed Q^2 values greater than 0.5 while the other models had weak correlation. Consequently, These twelve models were chosen like the best.

Table 2 gathers the twelve best selected CoMFA/CoMSIA models and their statistical indicators. The CoMFA model explains the activity with contributions of steric fields of 56.6% and electrostatic fields of 43.4%. Among all the CoMSIA models generated, the best CoMSIA model explains the studied activity in terms of steric, and hydrophobic fields with contributions of 12.2 and 11.4% respectively. The statistical values of the optimal number of components (ONC), Q^2 , R^2 , and SEE, were 2, 0.538, 0.925, and 0.185 and 1, 0.593, 0.905, and 0.208 for the model CoMFA and CoMSIA, respectively.

It should be noted that the CoMSIA model showed the highest R^2_{pred} coefficient value than all the other models built and also higher than the CoMFA model itself. In this way, the CoMSIA model has higher predictive power than the CoMFA model. To further assess the predictive quality of models selected from structurally similar compounds, some statistical metrics were calculated on molecules of the test set [46]. The statistical results of the additional external validation of the selected CoMFA and CoMSIA models are listed in Table 3. The statistical criteria of Tropsha and

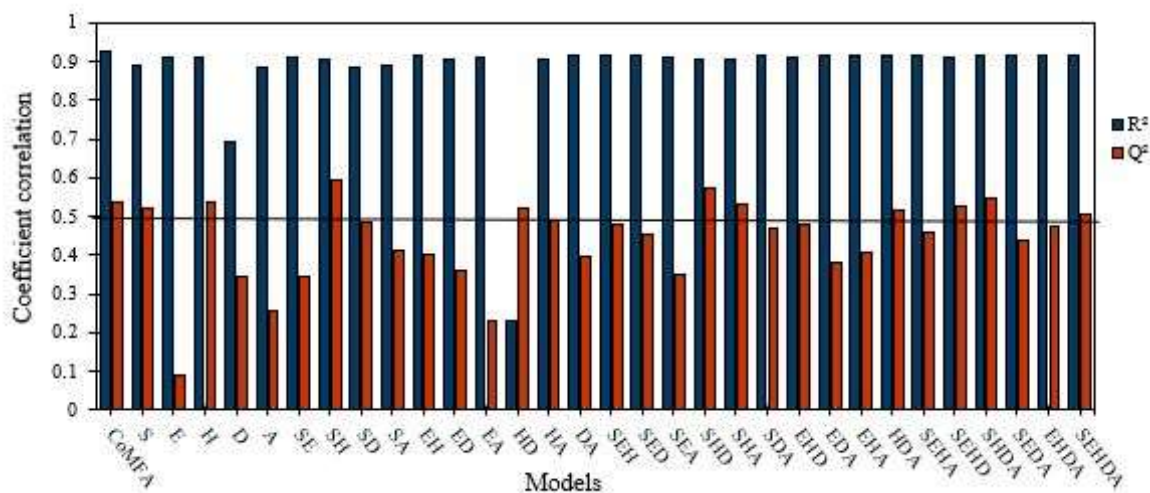


Fig. 2. Results of the 31 possible combinations of CoMSIA models and the CoMFA model according to their Q^2 and R^2 values.

Table 2. Statistical Results of CoMSIA Models with Different Combinations of Molecular Fields

Models	R ²	Q ²	SEE	F	ONC	R ² _{pred}	Contribution fractions					
							S	E	H	D	A	
CoMFA	0.925	0.538	0.185	32.802	1	0.867	0.566	0.434				
S	0.891	0.519	0.223	21.754	1	0.900	1					
H	0.908	0.537	0.204	26.419	2	0.251			1			
CoMSIA/SH	0.905	0.593	0.208	25.386	2	0.913	0.517		0.483			
CoMSIA/HD	0.884	0.523	0.23	20.265	1	0.339			0.553	0.447		
CoMSIA/HA	0.905	0.500	0.208	25.342	1	0.288			0.393		0.607	
CoMSIA/SHD	0.901	0.575	0.212	24.336	1	0.690	0.261		0.328	0.411		
CoMSIA/SHA	0.906	0.534	0.207	25.738	1	0.902	0.272		0.296		0.432	
CoMSIA/HDA	0.917	0.518	0.194	29.403	1	0.721			0.189	0.413	0.398	
CoMSIA/SEHD	0.913	0.526	0.199	28.061	1	0.802	0.193	0.295	0.187	0.325		
CoMSIA/SHDA	0.916	0.549	0.195	29.259	1	0.764	0.169		0.174	0.348	0.310	
CoMSIA/SEHDA	0.917	0.506	0.194	29.523	1	0.819	0.087	0.171	0.140	0.353	0.250	

The greatest model is indicated in bold.

Table 3. The Result of the Statistical Parameters of External Validation of the CoMFA and CoMSIA (SH) Models

Parameter	Acceptable range	3D-QSAR	
		CoMFA	CoMSIA/SH
r_0^2	>0.5	0,973	0,562
$r_0'^2$	>0.5	0,779	0,998
R ²	>0.6	0,867	0,913
k	0,85 < k < 1.15	1,015	0,945
$(R^2 - R_0^2)/R^2$	<0.1	-0,122	0,084
k'	0,85 < k' < 1.15	0,933	1,006
$(R^2 - R'^2_0)/R^2$	<0.1	0,102	-0,093
r_m^2	>0.5	0,585	0,572
$r_m'^2$	>0.5	0,609	0,647
\bar{r}_m^2	>0.5	0,597	0,502
Δr_m^2	<0.2	0,024	0,175
Δr_0^2	< 0.3	0,195	-0,436

Golbraikh were respected by all the generated models, also the Roy metrics Δr_m^2 and r_m^2 satisfied the requirements. The CoMSIA/SH model gave a higher value of R^2_{pred} than the

CoMSIA model (0.913 > 0.867), which confirms once again that the productivity of CoMSIA model is better than that of CoMFA model.

Graphical Interpretation of 3D QSAR Models

Contour maps for the selected models CoMFA and CoMSIA/SH were generated on the most active molecule (N°22). The maps of steric and hydrophobic contours of CoMSIA are presented in Fig. 4a. In the steric map, the green and yellow outlines indicate regions favorable and unfavorable for biological activity for bulky substitution, respectively. Two green sectors near the R₂ and R₃ substitution implied that bulky groups in these positions could be decreased the activity. In particular, the contour near R₂ is widely open to accommodate larger groups, that's why compound N°20 (R₂ = Methyl) with larger groups at this position is more active than compound N°27 (R₂ = H). The yellow outline near the substituted methoxy group R₂ indicated that large groups at this position could decrease activity. Another yellow outline at the terminal end of the R₂ substitution shows that prolonged groups are disadvantageous there.

The CoMFA electrostatic contour map is shown in Fig. 4b. The red outlines imply regions favorable to electron donor substitution while the blue outlines indicate regions favorable to acceptor electron substitutions. Three principles blue sectors are located near position 7 of the indole group, near oxygen atom of substituent R₂ and on the terminal end of substitution, R₃ indicated that electron-rich groups at these positions may decrease activity. Two small red outlines near the R₁ substitution and R₁ substitution mean that electronegative atoms at these positions can increase activity. On the CoMSIA model steric map, the green and yellow contours show the regions favorable and unfavorable to the biological activity for the bulky substitution, respectively. Two green contours are similar to those of the CoMSIA model contour map. The yellow outlines are localized on the R₂ substitution and near the nitrogen atom of indole groups which indicates small groups at these positions could enhance the activity Fig. 5a.

In the CoMSIA hydrophobic contour map as shown in Fig. 5b. The yellow and gray outlines represent the favorable regions for the hydrophobic group and hydrophilic group respectively. Two gray outline groups around the R₂ substitution and R₃ substitution indicate hydrophilic groups in those positions might have increased activity. In addition, two other gray areas around the R₁ substitution also show the need for the hydrophilic groups at this position to enhance activity.

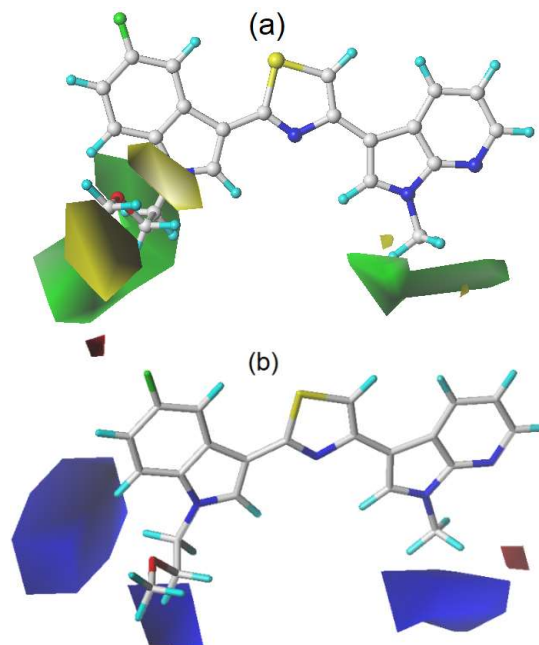


Fig. 4. Contour map of CoMFA analysis (a) Steric (b) electrostatic with a grid spacing of 2.0 Å in combination with compound N°22.

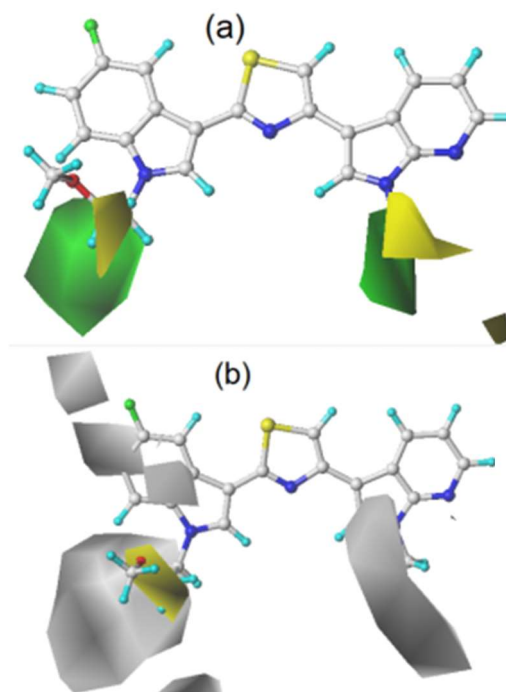


Fig. 5. Contour map of CoMSIA/SH analysis (a) Steric and (c) hydrophobic (d) hydrogen bonding donor with a grid spacing of 2.0 Å in combination with compound N°22.

Design newly Compounds

CoMFA and CoMSIA analysis was performed on thiazole derivatives for their antibiofilm activity. According to the results of the model validations, the CoMSIA model showed stronger predictive power than of CoMFA model, that is why we are based on the CoMSIA model and the analysis of its contour map to identify the target sites for improved inhibitory activity (pIC_{50}). The presence of large electropositive and hydrophobic groups attached to the pyrido-carboxamide ring and large electronegative groups to the pyrazole could make the compound a more potent inhibitor. Based on our results, we designed eleven compounds with predicted activities that were within the range of the most active compound. The structure and values

of predicted activities ($pIC_{50(pred)}$) of newly designed compounds using selected model are shown in Table 4. The new compounds showed similar and encouraging synthetic accessibility values.

ADME/toxicity Prediction and Analysis

The ADME/toxicity in silico properties of eleven newly designed compounds was estimated. The absorbance values of all the compounds are very high and much higher than 30% which indicates the strong absorption of these compounds[46]. Broadcast Volume (VDss) represents the drug dilution space, it was greater than 0.45, so it is considered high, except for compound Pred08 where it was low Table 5.

Table 4. Predicted Activities and Affinity for the Eleven Compounds Newly Designed and the Compound most Active

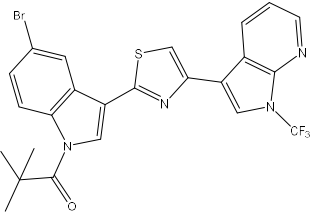
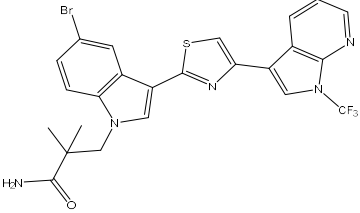
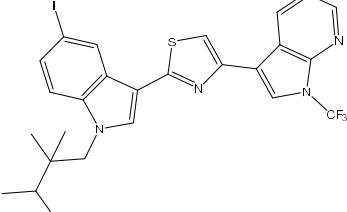
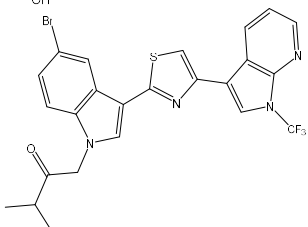
Comp.	Structure	CoMSIA $pIC_{50(pred)}$	Affinity (kcal mol ⁻¹)	Synthetic asseccibility
Pred01		7.076	-8.0	3.73
Pred02		6,817	-8.5	3.68
Pred03		6.813	-8.7	3.93
Pred04		6.792	-8.3	3.62

Table 4. Continued

Pred05		6.764	-7.9	3.71
Pred06		6.723	-8.2	3.73
Pred07		6.683	-7.8	3.47
Pred08		6.638	-8.2	3.76
Pred09		6.589	-8.0	3.66
Pred10		6.573	-8.5	3.77
Pred11		6.481	-8.3	3.84
N°22	-	5.131	-7.3	3.47

Table 5. ADME Properties of Newly Designed Compounds Based on the CoMSA/SH Model

Comp. N°	Absorption			Distribution		Metabolism					Excretion
	Water Solubility	Intestinal absorption (Human)	Skin Permeability	VD _{ss} (Human)	BBB Permeability	CYP2D6	CYP3A4	CYP1A2	CYP2D6	CYP3A4	Total clearance
						Substrate			Inhibitor		
	logM	%	logK _p	logL/kg	logBB	Yes/No	Yes/No	Yes/No	Yes/No	Yes/No	log ml/min/kg
Pred01	-5.152	93.883	-2.726	1.015	-2.726	No	Yes	No	No	Yes	0.339
Pred02	-4.576	93.674	-2.728	0.944	-1.524	No	Yes	No	No	Yes	0.076
Pred03	-4.566	92.438	-2.73	0.976	0.338	No	Yes	No	No	Yes	-0.054
Pred04	-5.05	94.399	-2.724	1.01	0.189	No	Yes	No	No	Yes	0.365
Pred05	-3.842	100	-2.736	0.66	-1.691	No	Yes	No	No	Yes	0.253
Pred06	-5.032	95.582	-2.728	0.797	-1.305	No	Yes	No	No	Yes	0.33
Pred07	-4.492	95.282	-2.728	0.659	0.350	No	Yes	No	No	Yes	0.359
Pred08	-3.267	92.787	-2.736	-0.062	-2.601	No	No	No	No	No	0.167
Pred09	3.872	100	-2.737	0.727	-1.49	No	Yes	No	No	Yes	0.113
Pred10	-4.402	100	-2.734	0.742	-1.825	No	Yes	No	No	Yes	0.254
Pred11	-5.106	94.042	-2.727	1.171	0.228	No	Yes	No	No	Yes	0.245
N22	-4.08	98.415	-2.739	0.841	-0.368	No	Yes	Yes	No	Yes	0.477

The toxicity criterion of new candidates is a highly curative factor. In this work, the AMES test showed that almost all the compounds were non-mutagenic and non-carcinogenic. Furthermore, the acute toxicity (LD₅₀) of the new compounds reached from 2.321 to 3.154 mol kg⁻¹, while the chronic toxicity (LOAEL) of the compounds was close (0.3 to 0.895 mg/kg body weight/day). Generally, all candidate compounds show no skin sensitization Table 6.

Docking Molecular Results

To investigate how compounds bind to the target

receptor, we performed molecular docking to determine the appropriate conformation in the binding site, also to identify therapeutic residues involved in the ligand/receptor interaction. The autock vina program was used to generate nine conformations, among these conformations the best conformation was chosen, the one that shows low binding energy.

Table 1 represents the affinity value of all the compounds in the data set. Generally, the affinity values range between -6.6 kcal mol⁻¹ and -8.1 kcal mol⁻¹, where compounds N°2, N°3, and N°4 had a higher affinity towards the protein

Table 6. Toxicity Profile of Newly Designed Compounds Based on CoMSA/SH Model Selected

Comp. N°	AMES toxicity	Max. tolerated dose (Human)	hERG I inhibitor	hERG II inhibitor	Oral rat acute toxicity (LD50)	Oral rat chronic toxicity (LOAEL)	Skin sensitisation	T. pyriformis toxicity	Minnow toxicity
	Yes/No	log mg/kg/day	Yes/No	Yes/No	mol kg ⁻¹	log mg/kg _{bw} /day	Yes/No	logug/L	logmM
Pred01	No	0.085	No	Yes	2.484	0.592	No	0.286	-0.504
Pred02	No	0.178	No	Yes	2.525	0.74	No	0.286	-0.036
Pred03	No	-0.026	No	Yes	2.650	0.664	No	0.286	0.755
Pred04	No	0.033	No	yes	2.401	0.592	No	0.287	-0.238
Pred05	No	0.292	No	Yes	2.954	0.509	No	0.286	2.149
Pred06	No	0.117	No	Yes	2.488	0.895	No	0.286	-0.019
Pred07	No	-0.162	No	No	2.321	0.653	No	0.286	0.227
Pred08	No	0.488	No	Yes	3.154	0.300	No	0.285	0.390
Pred09	No	0.272	No	Yes	2.947	0.664	No	0.286	1.934
Pred10	Yes	0.313	No	Yes	3.091	0.476	No	0.285	0.022
Pred11	No	0.068	No	Yes	2.454	0.623	No	0.286	-0.468
N22	No	0.259	No	Yes	2.181	0.402	No	0.286	-1.059

binding site (8.1 kcal mol⁻¹). Table 4 groups together the affinity of the proposed candidates where they showed affinity values which exceed 8.1 kcal mol⁻¹, for example, the compound Pred03 with a value of 8.7 kcal mol⁻¹.

To better understand the interactions of compounds in the target protein binding site four systems were selected, the most active compound, the least active, the co-crystallized ligand, and the newly predicted pred01 compound. Figure 1 illustrates the result of the 2D and 3D interactions of the compounds screened.

Compound N°22 is delimited by a binding pocket consisting of residues Gln-93, His-132, Asp-151, Phe-154, Arg-160, Phe-163, and His-192. In addition, the compound N°22 forms certain hydrogen bonding interactions in the binding site between Gln-93 and the nitrogen atom of substituent R₂ and between Arg-160 and fluorine at a distance of 2.38 and 5.53 Å, respectively. The interactions of N08 compounds are formed with the residues Asp-60, His-61, Trp-86, Met-96, Phe-97, Asp-151, and Arg-160 as shown in Fig. 6. The specific hydrogen bond interactions are observed between Asp-60 and Asp-151 and the two hydrogens of nitrogen atoms of substitute R₂ at a distance of 3.88 and

4.69 Å, respectively. But it should be pointed out that the presence of unfavorable interaction of a hydrogen bond with the same hydrogen of nitrogen atoms and the His61 residue causes the low stability of this complex which justifies the low activity of this compound among the most compounds of the data set. In the case of the newly designed compound Pred01, the interactions displayed in the binding pocket are His-58, Trp-86, Ala-192, Met-96, Phe-97, Phe-154, Arg-160, Phe-163, Pro-164, and His-192. A hydrogen bond was marked between His-192 and the acetone group oxygen atom inserted at a distance of 2.60 Å. It should be noted that the residue His-192 was involved in the co-crystalline bonding reaction in the form of a hydrogen bond, along with the residue His-58.

As validate our docking result, a re-docking technique was conducted to the referential ligand, superimposing the re-docked ligand (red) and the referential ligand (yellow). As appeared in Fig. 7, the two ligands are almost superimposed. Additionally, the low root mean square deviation (RMSD) between the reference ligand and the re-docked ligand was in the order of 1.218 Å, suggesting that this protocol is most suitable to recreate the ligand's natural binding mode in the

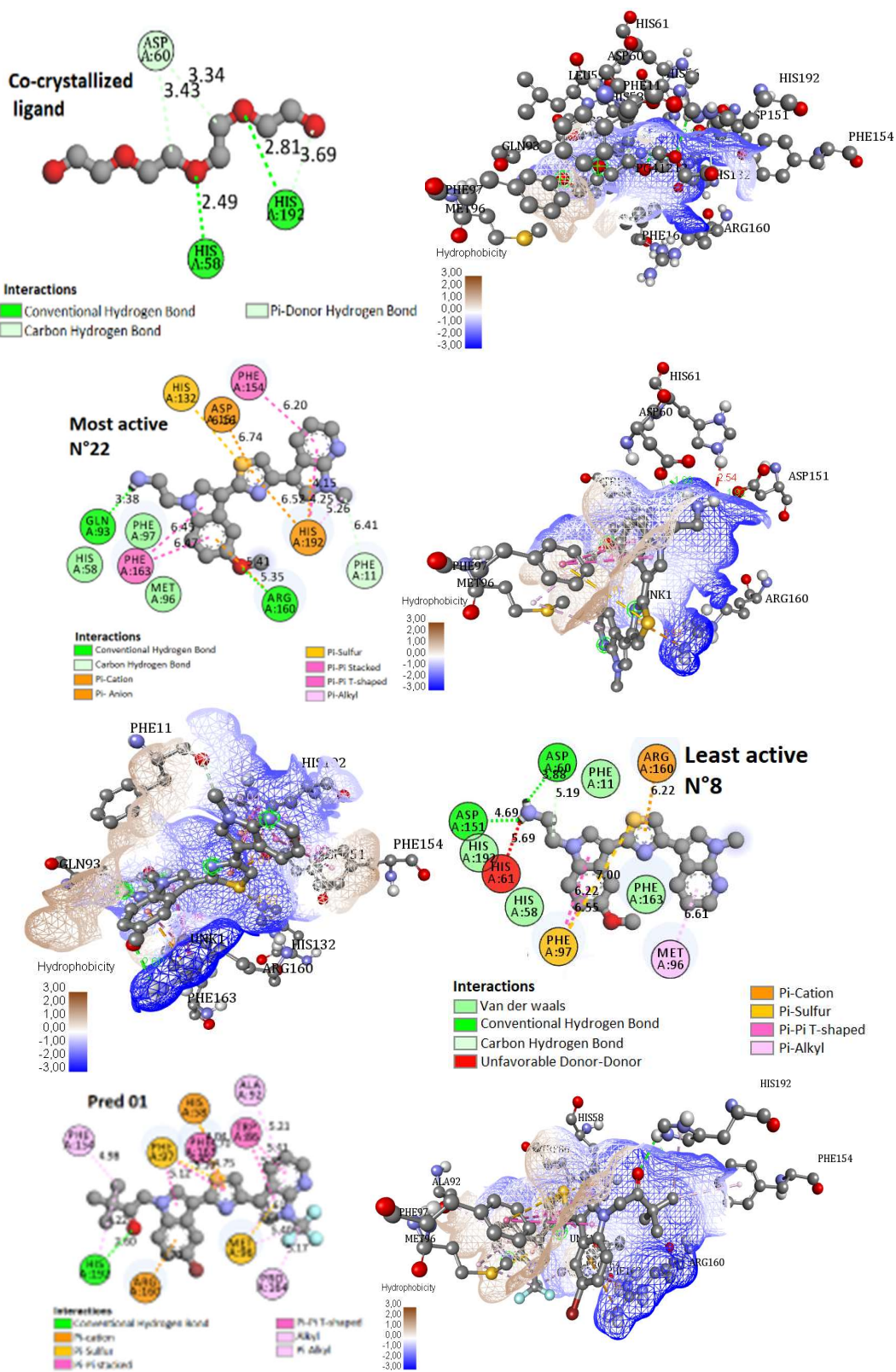


Fig. 6. 2D and 3D interactions of compounds reference ligand, N°22, N°08, and Pred01 newly designed by CoMSIA model in the binding site.

protein binding site.

MD Simulations Results

Since protein-ligand interaction *in vivo* is a dynamic process, the results obtained by docking are inconclusive. For this reason, we call the MD simulations, to assess the dynamic stability of modeled protein-ligand complex, particularly under biological system conditions, and reinforce our results. MD simulations were performed for three complex systems: the most active compound N08, the least active compound N°22, and the predicted compound Pred01. This study was carried out in terms of RMSD, RMSF, and Rg, to dynamically understand the interaction ligand/receptor. The behavior of analyzes depends on simulation time for this, we have simulated the selected system during a time of 100 ns. The conformational change of receptor during MD trajectory was estimated by calculating the RMSD backbone atoms. As shown in Fig. 8, the backbone RMSD values indicated that Compound N°22 and Pred01 complex increased steadily for the first 62 ns, then both systems reach equilibrium for the remainder of the simulation time. Since the variations in RMSD were kept to less than 0.3 nm, this indicates that these systems reached equilibrium during MD simulations at 100 ns.

In addition, the compactness of the protein was estimated by measuring the Rg. These parameters express the squared distance between the root and mass of the anatomy group from their common centre of mass [47]. Rg anisotropy values along the MD path are shown in Fig. 9. For these two complexes, Rg values are approximately stable in the first 50 ns. Around 60 ns, the complex corresponding to Pred01 shows a small Rg deformation, then returns stable in the last 20 ns of simulation time and remains confused with that of the complex corresponding to compound N°22.

The flexibility of the protein backbone was examined by following the RMSF values Fig. 10. The RMSF values for the Pred01 complex are low compared to those of the N°22 complex, a peak appears at the residue of number 1500 for the two complexes but for the Pred01 complex is less weak than the N°22 complex; Thus, we conclude that the Pred01 complex is less flexible and that it is of good complex compared to the N°22 complex. Great flexibility at the end of the protein is justified by the binding of compounds with the protein.

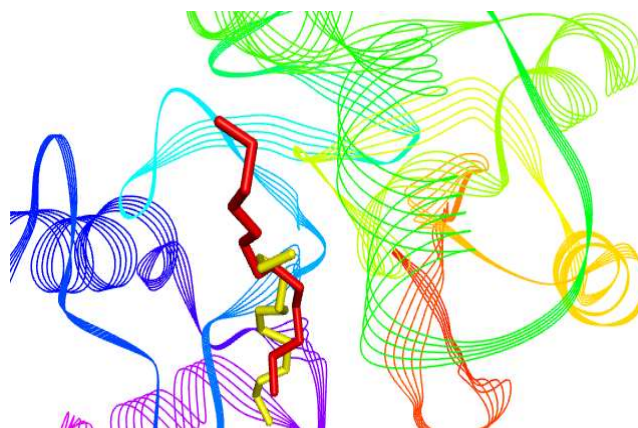


Fig. 7. Redocking of the co-crystallized ligand (red) and the docked ligand (yellow) to protein (PDB: 2XF).

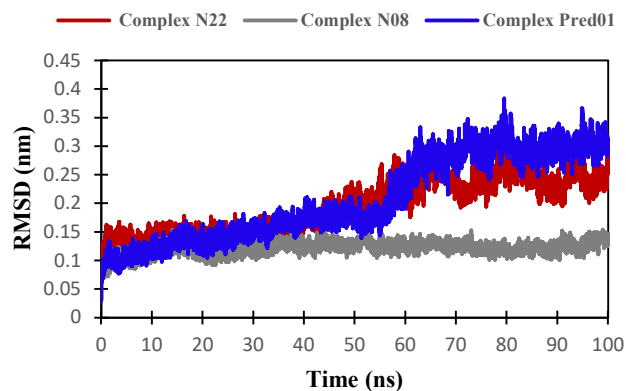


Fig. 8. RMSD graphs of the receptor backbone in complex ligand according to the simulation.

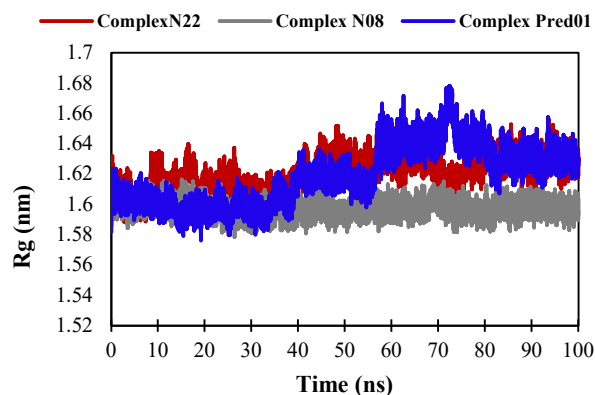


Fig. 9. The gyration radius plot of receptor/ligand of screened compounds.

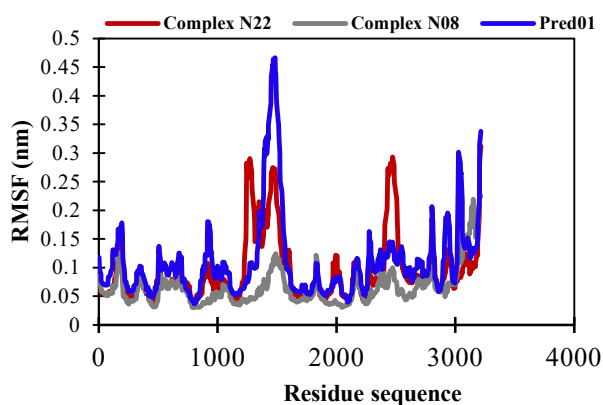


Fig. 10. RMSF graph of the receptor in complex with compound screened according to the simulation.

Binding Energy Calculation

From the results obtained by the MM-PBSA method, the average binding free energies (ΔG_{Bind}) of complexes N^o22, N^o08, and Pred01 calculated during the 100 ns simulation were found to be -14.966 ± 32.97 kJ mol⁻¹ and -17.190 ± 27.10 kJ mol⁻¹ and -43.075 kJ mol⁻¹, respectively. The details of the MM-PBSA calculation of the complexes are summarized in Table 7.

In Table 7 The calculated averages of the molecular mechanic's potential energy (ΔE_{MM}), polar solvation energy (ΔG_{Polar}), and non-polar solvation energy ($\Delta G_{\text{Non-polar}}$ or ΔG_{SASA}) under ΔG_{PB} between the protein and ligand during the simulation were evaluated from the MM-PBSA calculation. The average ΔE_{MM} for complexes N^o22, N^o08, and Pred 01 were found to be -40.023 ± 48.622 and

-51.148 ± 74.55 and -86.911 ± 63.033 kJ mol⁻¹, respectively, and the average value of ΔG_{Polar} for the N^o22 complex, N^o08 complex and Pred01 complex were -29.560 ± -32.630 , -73.819 ± -84.19 , and 52.140 ± 43.663 kJ mol⁻¹, respectively. The calculated average $\Delta G_{\text{Non-polar}}$ or ΔG_{SASA} for N^o22 complex, N^o08 complex and Pred 01 were found to be -4.503 ± 5.022 , -5.482 ± 7.497 , and -8.304 ± 5.241 kJ mol⁻¹, respectively.

Density Functional Theory Analysis

Frontier molecular orbital analysis of the most active (N^o22), least active (N^o08) compounds and the newly designed Pred01 were evaluated to understand their electronic profiles and to predict electrophilic or nucleophilic reactive sites. The values of the overall molecular reactivity descriptors of compounds N^o22, N^o08, and Pred01 were calculated and grouped in Table 8, to predict the tendency of a compound to engage in drug interactions and also to explain their chemical properties and reactivity [48].

As shown in Table 8, the values of ionization potential were 5.129, 4.770, and 5.495, the values of electron affinity were 1.116, 0.710, and 1.510, and the Energy gap was 4.012 eV, 4.059 eV, and 3.985 eV for compounds N^o22, N^o08, and Pred01, respectively. The low electrophilicity values of three compounds indicate their greater tendency to interact with nucleophilic sites. The ionization potential is minimum for N^o08 and maximum for Pred01. The results show that the gap of the border orbitals of three compounds is less than 5, which is evidence of stronger interaction with the receptor. It is evident that the newly designed compound Pred01 has the

Table 7. MM-PBSA Calculation

Protein-ligand complexes	ΔE_{MM} (kJ mol ⁻¹)		ΔG_{Sol} (kJ mol ⁻¹)		Binding energy (kJ mol ⁻¹)
	Van der Waal	Electrostatic	Polar solvation	SASA energy	
	Energy (kJ mol ⁻¹)		Energy (kJ mol ⁻¹)		
Complex N ^o 22	-35.694 ± 39.199	-4.329 ± 9.423	29.560 ± 32.630	-4.503 ± 5.022	-14.966 ± 40.068
Complex N ^o 08	-49.541 ± 66.309	-1.607 ± 8.241	73.819 ± 84.191	-5.482 ± 7.497	17.190 ± 42.283
Complex Pred01	-67.423 ± 41.596	-19.488 ± 21.437	52.140 ± 43.663	-8.304 ± 5.241	-43.075 ± 40.624

Table 8. Calculated Electronic Properties of for the Screened Bioactive Compounds Using the B3LYP/6-31G Method

Compounds	N°22	N°08	Pred01
IP (ev)	5.129	4.770	5.495
EA (ev)	1.116	0.710	1.510
E _{Gap} (ev)	4.012	4.059	3.985
Electrophilie global ω (ev)	1.215	0.925	6.157
Energy change ΔE (ev)	-1.215	-0.925	-6.157
Softness σ (ev)	0.249	0.246	0.251
Hardness η (ev)	4.012	4.059	3.985
Chemical potential μ (ev)	-3.122	-2.740	-7.005
Electronegativity χ (ev)	3.122	2.740	7.005

smallest energy gap which shows that is more polarizable and generally more chemically reactive. Furthermore, these results explain the charge transfer interactions that are indicated in the study of molecular docking which enhances the activity. E_{HOMO}/E_{LUMO} plots of the screened compounds gathered in Fig. 11.

The electron affinity is higher for Pred01 but is less low for compound N°08, which indicates that this last compound has less tendency to gain electrons, while Pred01 is more inclined to gain electrons. The values of chemical harness (η) and energy of exchange were calculated to be 4.012 ev, 4.059 ev, and 3.985 ev; -1.215 ev, -0.925 ev, and -6.157 ev for compounds N°22, N°08, and Pred01, respectively. These results show that the charge transition process is desirable in terms of energy. The suitability of these values for the studied compounds suggests that they have a tendency to interact with the acceptor as a bioactive compound. The softness (s) varies in the order Pred01 > N°22 > N°08. The Chemical potential is the energy available in the system to do useful work. The chemical potential values, which are a very useful indicator of the reactivity of compounds, indicated that the lower value is for N°08 and the higher value is for the Pred01. This shows that Pred01 is more reactive compared to the two compounds. The energy difference decreases in the order N°08 > N°22 > Pred01.

Figure 12 shows the frontier orbital map of more and less active complexed compounds. The red color region indicates negative charges and the blue color region indicates a

positive charge area.

Additionally, the electrostatic potential of the molecule was computed using the distribution of its surface charges. As a result, the DFT calculation used the atomic charge surrounding the screened compounds to generate the electrostatic potential map based on the Mulliken population analysis [49]. Figure 13 shows the negative and positive regions of electrostatic potentials and hydrogen bond interactions as well as the shape and size of ligands in terms of color outline, in which the blue outline followed by green represents the electropositive and the orange and red outline represents the electronegative as indicated on the MESP maps.

Thus Fig. 13 shows the 3D contours of the MESP clearly support that the nitrogen group is primarily responsible for the biological activity studied. In general, it is obvious that the MESP card does not affect when the phenyl ring has been substituted in the electronic properties of bicyclic rings.

CONCLUSIONS

In this research paper, we applied a combined approach of 3D-QSAR, docking molecular, DFT, and MD studies to understand the structural basis and mechanism of inhibition of thiazole derivatives as biofilm inhibitors. The developed 3D-QSAR model resulted in high predictive ability with a training set of $R^2_{\text{Pred}} = 0.98$ and $SEE = 0.07$ and a test set of $Q^2 = 0.89$, $SEE = 0.14$ and $R^2_{\text{pred}} = 0.90$. These results provide

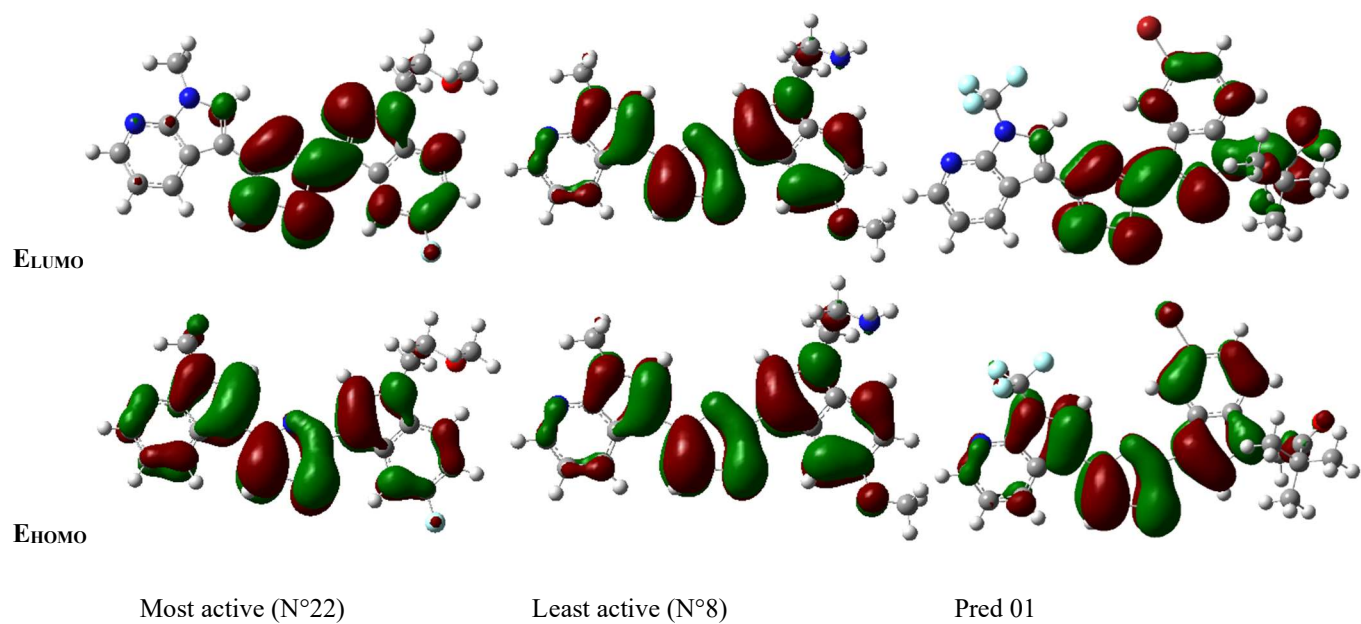


Fig. 11. The optimized structures, E_{HOMO} , E_{LUMO} of thiazole inhibitor molecules using DFT/B3LYP/6-31G on compounds N°22, N°08, and Pred 01.

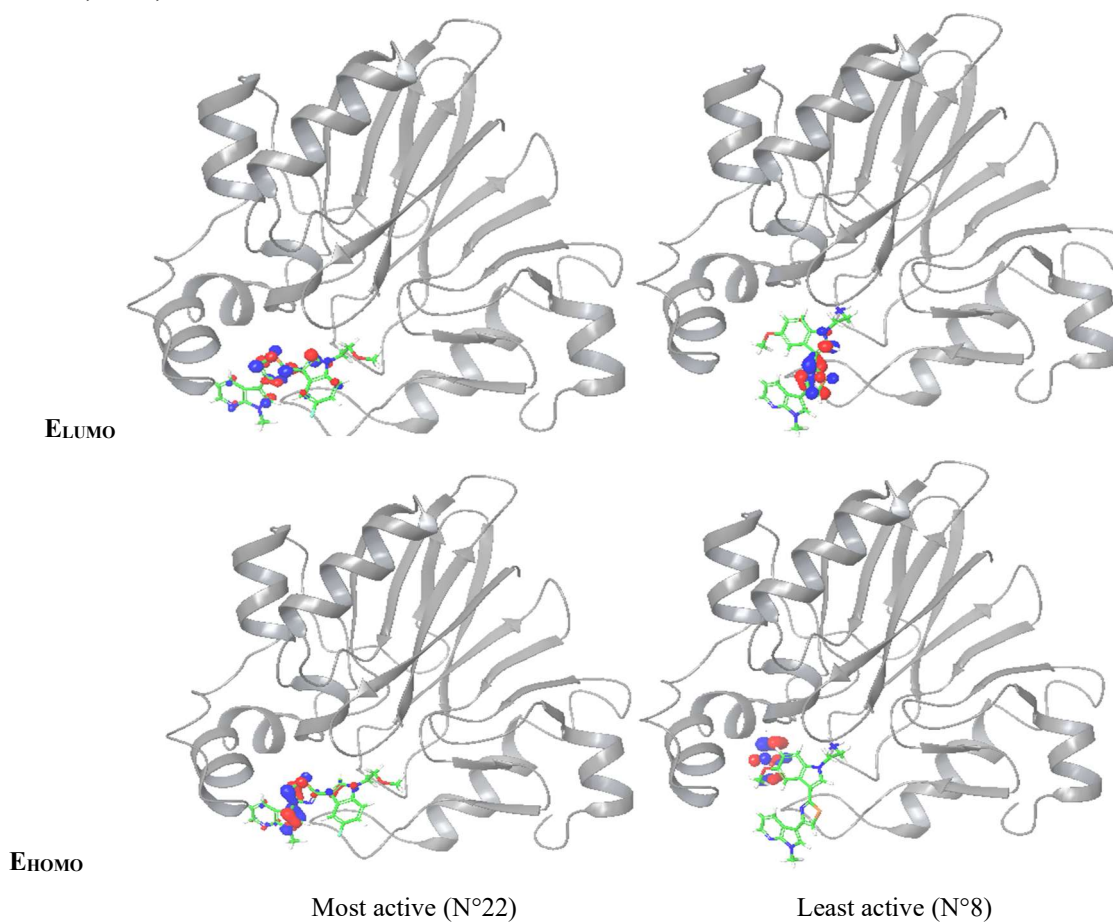


Fig. 12. Map of frontier orbitals (E_{HOMO} and E_{LUMO}) of complex most and least active activity.

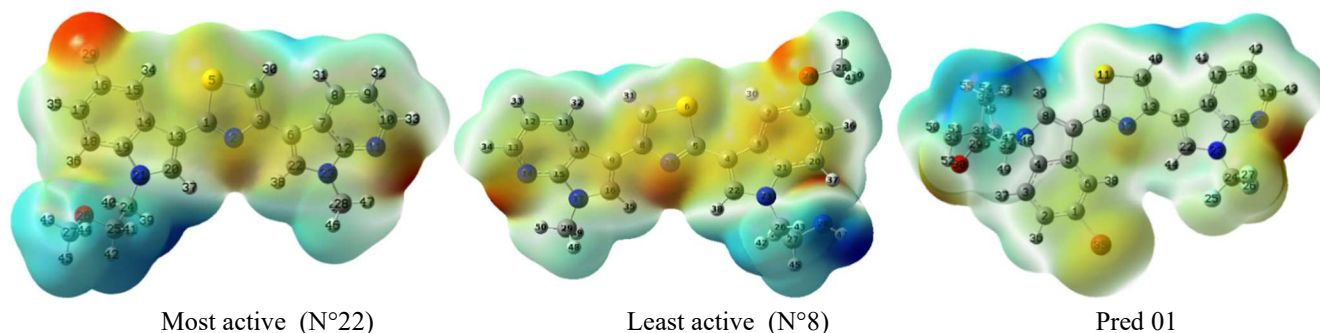


Fig. 13. Representation of molecular electrostatic potential structures (MESP) on compounds N°22, N°8, and Pred 01.

a solid information base for evaluating the structure-activity relationship of thiazole derivatives. Molecular docking analysis shows the types of interactions and the nature of the residues involved in the activity studied. The proposed molecules were then analyzed for their ADME/toxicity and showed acceptable results. Moreover, the stability of the model was evaluated using MD simulations accompanied by calculating the binding free energy, DFT studies were carried out to clearly describe the energy profiles of the studied compounds. Therefore, eleven proposed compounds were found to be more stable in the target protein binding site. Thus, we point out that these findings may be a potential lead for the advancement of novel biofilm inhibitors for antibiotics treatment. Finally, these results, when taken together, help in a better understanding of ligand-receptor interactions, which contributes in the discovery, development, and designing of biofilm.

ACKNOWLEDGEMENTS

We are grateful to the “Association Marocaine des Chimistes Théoriciens” (AMCT) for its pertinent help concerning the programs.

REFERENCES

- [1] Attinger, C.; Wolcott, R., Clinically Addressing Biofilm in Chronic Wounds. *Advances in Wound Care* **2012**, *1*, 127-132. <https://doi.org/10.1089/wound.2011.0333>.
- [2] Römling, U.; Balsalobre, C., Biofilm Infections, Their Resilience to Therapy and Innovative Treatment Strategies. *Journal of Internal Medicine* **2012**, *272*(6), 541-561. <https://doi.org/10.1111/joim.12004>.
- [3] Jamal, M.; Ahmad, W.; Andleeb, S.; Jalil, F.; Imran, M.; Nawaz, M. A.; Hussain, T.; Ali, M.; Rafiq, M.; Kamil, M. A., Bacterial Biofilm and Associated Infections. *Journal of the Chinese Medical Association* **2018**, *81*(1), 7-11. <https://doi.org/10.1016/j.jcma.2017.07.012>.
- [4] Blair, J.; Webber, M. A.; Baylay, A. J.; Ogbolu, D. O.; Piddock, L. J., Molecular Mechanisms of Antibiotic Resistance. *Nat. Rev. Microbiol.* **2015**, *13*(1), 42-51. <https://doi.org/10.1038/nrmicro3380>.
- [5] Sun, W.; Han, Y.; Li, Z.; Ge, K.; Zhang, J., Bone-Targeted Mesoporous Silica Nanocarrier Anchored by Zoledronate for Cancer Bone Metastasis. *Langmuir* **2016**, *32*(36), 9237-9244. <https://doi.org/10.1021/acs.langmuir.6b02228>.
- [6] Walker, J. J.; Spear, J. R.; Pace, N. R., Geobiology of a Microbial Endolithic Community in the Yellowstone Geothermal Environment. *Nature* **2005**, *434*(7036), 1011-1014. <https://doi.org/10.1038/nature03447>.
- [7] López, D.; Vlamakis, H.; Kolter, R., Biofilms. *Cold Spring Harbor Perspectives in Biology* **2010**, *2*(7), a000398. <https://doi.org/10.1101/cshperspect.a000398>.
- [8] Monds, R. D.; O'Toole, G. A., The Developmental Model of Microbial Biofilms: Ten Years of a Paradigm up for Review. *Trends in Microbiology* **2009**, *17*(2), 73-87. <https://doi.org/10.1016/j.tim.2008.11.001>.
- [9] Fulaz, S.; Vitale, S.; Quinn, L.; Casey, E. Nanoparticle-Biofilm Interactions: The Role of the EPS Matrix. *Trends in Microbiology* **2019**, *27*(11), 915-926. <https://doi.org/10.1016/j.tim.2019.07.004>.

- [10] Verderosa, A. D.; Totsika, M.; Fairfull-Smith, K. E., Bacterial Biofilm Eradication Agents: A Current Review. *Frontiers in Chemistry* **2019**, 824. <https://doi.org/10.3389/fchem.2019.00824>.
- [11] Bjarnsholt, T.; Alhede, M.; Alhede, M.; Eickhardt-Sørensen, S. R.; Moser, C.; Kühl, M.; Jensen, P. Ø.; Hoiby, N., The *In Vivo* Biofilm. *Trends in Microbiology* **2013**, 21(9), 466-474. <https://doi.org/10.1016/j.tim.2013.06.002>.
- [12] Van Acker, H.; Van Dijk, P.; Coenye, T., Molecular Mechanisms of Antimicrobial Tolerance and Resistance in Bacterial and Fungal Biofilms. *Trends in Microbiology* **2014**, 22(6), 326-333. <https://doi.org/10.1016/j.tim.2014.02.001>.
- [13] Pontes, J. T. C. de; Toledo Borges, A. B.; Roque-Borda, C. A.; Pavan, F. R., Antimicrobial Peptides as an Alternative for the Eradication of Bacterial Biofilms of Multi-Drug Resistant Bacteria. *Pharmaceutics* **2022**, 14(3), 642. <https://doi.org/10.3390/pharmaceutics14030642>.
- [14] Strathdee, S. A.; Davies, S. C.; Marcelin, J. R., Confronting Antimicrobial Resistance beyond the COVID-19 Pandemic and the 2020 US Election. *The Lancet* **2020**, 396(10257), 1050-1053. [https://doi.org/10.1016/S0140-6736\(20\)32063-8](https://doi.org/10.1016/S0140-6736(20)32063-8).
- [15] Schillaci, D.; Spinello, A.; Cusimano, M. G.; Cascioferro, S.; Barone, G.; Vitale, M.; Arizza, V., A Peptide from Human β Thymosin as a Platform for the Development of New Anti-Biofilm Agents for Staphylococcus Spp. and Pseudomonas Aeruginosa. *World J. Microbiol. Biotechnol.* **2016**, 32(8), 1-9. <https://doi.org/10.1007/s11274-016-2096-2>.
- [16] Tabti, K., QSAR Studies of New Compounds Based on Thiazole Derivatives as PIN1 Inhibitors via Statistical Methods. *RHAZES: GAC.* **2020**, 9, 70-91. <https://doi.org/10.48419/IMIST.PRSM/rhazes-v9.21394>
- [17] Joshi, D.; Yadav, S.; Sharma, R.; Pandya, M.; Bhadauria, R. S., Molecular Modelling Studies on Thiazole-Based α -Glucosidase Inhibitors Using Docking and CoMFA, CoMSIA and HQSAR. *Curr. Drug Discov. Technol.* **2021**, 18(6), 42-57. <https://doi.org/10.2174/1570163817666201022111213>
- [18] Tabti, K.; Elmchichi, L.; Sbai, A.; Maghat, H.; Bouachrine, M.; Lakhlifi, T.; Ghosh, A., *In Silico* Design of Novel PIN1 Inhibitors by Combined of 3D-QSAR, Molecular Docking, Molecular Dynamic Simulation and ADMET Studies. *J. Mol. Struct.* **2022**, 1253, 132291. <https://doi.org/10.1016/j.molstruc.2021.132291>.
- [19] Hajji, H.; Tabti, K.; En-nahli, F.; Bouamrane, S.; Lakhlifi, T.; Ajana, M. A.; Bouachrine, M., *In Silico* Investigation on the Beneficial Effects of Medicinal Plants on Diabetes and Obesity: Molecular Docking, Molecular Dynamic Simulations, and ADMET Studies. *Biointerface Res. Appl. Chem.* **2021**, 11(5), 6933-6949. <https://doi.org/10.33263/BRIAC115.69336949>.
- [20] Zhao, J.; Liu, M.; Zang, J.; Yang, S.; Chen, R.; Zhao, X.; Ding, L., Molecular Docking, 3D-QASR and Molecular Dynamics Simulations of Thiazoles Pin1 Inhibitors. *J. Biomol. Struct. Dyn.* **2021**, 1-15. <https://doi.org/10.1080/07391102.2021.1975568>.
- [21] Elkarhat, Z.; Charoute, H.; Elkhatabi, L.; Barakat, A.; Rouba, H., Potential Inhibitors of SARS-Cov-2 RNA Dependent RNA Polymerase Protein: Molecular Docking, Molecular Dynamics Simulations and MM-PBSA Analyses. *J. Biomol. Struct. Dyn.* **2022**, 40(1), 361-374. <https://doi.org/10.1080/07391102.2020.1813628>
- [22] Obakachi, V. A.; Kehinde, I.; Kushwaha, N. D.; Akinpelu, O. I.; Kushwaha, B.; Merugu, S. R.; Kayamba, F.; Kumalo, H. M.; Karpoomath, R., Structural Based Investigation of Novel Pyrazole-Thiazole Hybrids as Dual CDK-1 and CDK-2 Inhibitors for Cancer Chemotherapy. *Mol. Simul.* **2022**, 1-15. <https://doi.org/10.1080/08927022.2022.2045016>.
- [23] Carbone, A.; Parrino, B.; Cusimano, M. G.; Spanò, V.; Montalbano, A.; Barraja, P.; Schillaci, D.; Cirrincione, G.; Diana, P.; Cascioferro, S., New Thiazole Nortopsentin Analogues Inhibit Bacterial Biofilm Formation. *Mar. Drugs* **2018**, 16(8), 274. <https://doi.org/10.3390/md16080274>.
- [24] Bai, F.; Liu, X.; Li, J.; Zhang, H.; Jiang, H.; Wang, X.; Li, H., Bioactive Conformational Generation of Small Molecules: A Comparative Analysis between Force-Field and Multiple Empirical Criteria Based Methods. *BMC Bioinform.* **2010**, 11(1), 1-12. <https://doi.org/10.1186/1471-2105-11-545>.

- [25] Wu, L.; Wang, Y.; Liu, Y.; Yu, S.; Xie, H.; Shi, X.; Qin, S.; Ma, F.; Tan, T. Z.; Thiery, J. P., A Central Role for TRPS1 in the Control of Cell Cycle and Cancer Development. *Oncotarget* **2014**, 5(17), 7677. <https://doi.org/10.18632/oncotarget.2291>.
- [26] Srivastava, V.; Kumar, A.; Mishra, B. N.; Siddiqi, M. I., CoMFA and CoMSIA 3D-QSAR Analysis of DMDP Derivatives as Anti-Cancer Agents. *Bioinformation* **2008**, 2(9), 384. <https://doi.org/10.6026/97320630002384>.
- [27] Bender, A.; Glen, R. C., Molecular Similarity: A Key Technique in Molecular Informatics. *Org. Biomol. Chem.* **2004**, 2(22), 3204-3218. <https://doi.org/10.1039/B409813G>.
- [28] Sheng, C.; Zhang, W.; Ji, H.; Zhang, M.; Song, Y.; Xu, H.; Zhu, J.; Miao, Z.; Jiang, Q.; Yao, J., Structure-Based Optimization of Azole Antifungal Agents by CoMFA, CoMSIA, and Molecular Docking. *J. Med. Chem.* **2006**, 49(8), 2512-2525. <https://doi.org/10.1021/jm051211n>.
- [29] Pearlstein, R. A.; Vaz, R. J.; Kang, J.; Chen, X.-L.; Preobrazhenskaya, M.; Shchekotikhin, A. E.; Korolev, A. M.; Lysenkova, L. N.; Miroshnikova, O. V.; Hendrix, J., Characterization of HERG Potassium Channel Inhibition Using CoMSIA 3D QSAR and Homology Modeling Approaches. *Bioorganic Med. Chem. Lett.* **2003**, 13(10), 1829-1835. [https://doi.org/10.1016/S0960-894X\(03\)00196-3](https://doi.org/10.1016/S0960-894X(03)00196-3).
- [30] Kruger, U.; Zhou, Y.; Wang, X.; Rooney, D.; Thompson, J., Robust Partial Least Squares Regression: Part I, Algorithmic Developments. *J. Chemom.* **2008**, 22(1), 1-13. <https://doi.org/10.1002/cem.1093>.
- [31] Tabti, K.; Sbai, A.; Maghat, H.; Bouachrine, M.; Lakhliifi, T., 2D and 3D-QSAR/CoMSIA Comparative Study On a Series of Thiazole Derivatives as SDHI Inhibitors. *Maghreb. J. Pure & Appl. Sci.* **2020**, 6(2), 73-90. <https://doi.org/10.48383/IMIST.PRSM/mjpas-v6i2.23108>.
- [32] Tabti, K.; Baammi, S.; Elmchichi, L.; Sbai, A.; Maghat, H.; Bouachrine, M.; Lakhliifi, T., Computational Investigation of Pyrrolidin Derivatives as Novel GPX4/MDM2-P53 Inhibitors Using 2D/3D-QSAR, ADME/Toxicity, Molecular Docking, Molecular Dynamics Simulations, and MM-GBSA Free Energy. *Struct. Chem.* **2022**, 1-21. <https://doi.org/10.1007/s11224-022-01903-5>.
- [33] Sridhar, J.; Foroozesh, M.; Stevens, C. K., QSAR Models of Cytochrome P450 Enzyme 1A2 Inhibitors Using CoMFA, CoMSIA and HQSAR. *SAR and QSAR Environ. Res.* **2011**, 22(7-8), 681-697. <https://doi.org/10.1080/1062936X.2011.623320>.
- [34] Berendsen, H. J.; Postma, J. P.; van Gunsteren, W. F.; Hermans, J., Interaction Models for Water in Relation to Protein Hydration. In *Intermolecular forces*; Springer, **1981**, pp. 331-342. https://doi.org/10.1007/978-94-015-7658-1_21.
- [35] Berendsen, H. J.; Postma, J. van; Van Gunsteren, W. F.; DiNola, A.; Haak, J. R., Molecular Dynamics with Coupling to an External Bath. *J. Chem. Phys.* **1984**, 81(8), 3684-3690. <https://doi.org/10.1063/1.448118>.
- [36] Parrinello, M.; Rahman, A. Polymorphic Transitions in Single Crystals: A New Molecular Dynamics Method. *J. Appl. Phys.* **1981**, 52(12), 718-7190. <https://doi.org/10.1063/1.328693>.
- [37] Essmann, U.; Perera, L.; Berkowitz, M. L.; Darden, T.; Lee, H.; Pedersen, L. G., A Smooth Particle Mesh Ewald Method. *J. Chem. Phys.* **1995**, 103(19), 8577-8593. <https://doi.org/10.1063/1.470117>
- [38] Kumari, R.; Kumar, R.; Consortium, O. S. D. D.; Lynn, A., G_mmpbsa□ A GROMACS Tool for High-Throughput MM-PBSA Calculations. *J. Chem. Inf. Model.* **2014**, 54(7), 1951-1962. <https://doi.org/10.1021/ci500020m>.
- [39] Baker, N. A.; Sept, D.; Joseph, S.; Holst, M. J.; McCammon, J. A., Electrostatics of Nanosystems: Application to Microtubules and the Ribosome. *Proc. Natl. Acad. Sci.* **2001**, 98(18), 10037-10041. <https://doi.org/10.1073/pnas.18134239>.
- [40] Mohapatra, R. K.; Perekhoda, L.; Azam, M.; Suleiman, M.; Sarangi, A. K.; Semenets, A.; Pintilie, L.; Al-Resayes, S. I., Computational Investigations of Three Main Drugs and Their Comparison with Synthesized Compounds as Potent Inhibitors of SARS-CoV-2 Main Protease (Mpro): DFT, QSAR, Molecular Docking, and in Silico Toxicity Analysis. *Journal of King Saud University-Science* **2021**, 33(2), 101315. <https://doi.org/10.1016/j.jksus.2020.101315>.
- [41] Saha, S. K.; Hens, A.; Murmu, N. C.; Banerjee, P., A Comparative Density Functional Theory and Molecular

- Dynamics Simulation Studies of the Corrosion Inhibitory Action of Two Novel N-Heterocyclic Organic Compounds along with a Few Others over Steel Surface. *J. Mol. Liq.* **2016**, *215*, 486-495. <https://doi.org/10.1016/j.molliq.2016.01.024>.
- [42] Taskin, D.; Ozdemir, M.; Yalcin, B., LC-ESI-Tandem MS and in Silico ADMET Analysis of Polyphenols from Rhus Coriaria L. and Micromeria Fruticosa (L.) Druce Ssp. Brachycalyx PH Davis. *Future J. Pharm. Sci.* **2021**, *7*(1), 1-11. <https://doi.org/10.1186/s43094-021-00317-0>.
- [43] Abdurrahman, S.; Ruslin, R.; Hasanah, A. N.; Mustarichie, R., Molecular Docking Studies and ADME-Tox Prediction of Phytocompounds from Merremia Peltata as a Potential Anti-Alopecia Treatment. *J. Adv. Pharm. Technol.* **2021**, *12*(2), 132. https://doi.org/10.4103/japtr.JAPTR_222_20.
- [44] Hou, T.; Wang, J.; Zhang, W.; Xu, X. ADME Evaluation in Drug Discovery. 7. Prediction of Oral Absorption by Correlation and Classification. *J. Chem. Inf. Mod.* **2007**, *47*(1), 208-218. <https://doi.org/10.1021/ci600343x>.
- [45] Bringmann, G.; Rummey, C., 3D QSAR Investigations on Antimalarial Naphthylisoquinoline Alkaloids by Comparative Molecular Similarity Indices Analysis (CoMSIA), Based on Different Alignment Approaches. *J. Chem. Inf. Model.* **2003**, *43*(1), 304-316. <https://doi.org/10.1021/ci025570s>.
- [46] Roy, K.; Ambure, P.; Aher, R. B. How Important Is to Detect Systematic Error in Predictions and Understand Statistical Applicability Domain of QSAR Models? *Chemom. Intell. Lab. Syst.* **2017**, *162*, 44-54. <https://doi.org/10.1016/j.chemolab.2017.01.010>.
- [47] Kumar, C. V.; Swetha, R. G.; Anbarasu, A.; Ramaiah, S., Computational Analysis Reveals the Association of Threonine 118 Methionine Mutation in PMP22 Resulting in CMT-1A. *Adv. Bioinform.* **2014**, *2014*. <https://doi.org/10.1155/2014/502618>.
- [48] Parthasarathi, R.; Subramanian, V.; Roy, D. R.; Chattaraj, P. K., Electrophilicity Index as a Possible Descriptor of Biological Activity. *Bioor. Med. Chem.* **2004**, *12*(21), 5533-5543. <https://doi.org/10.1016/j.bmc.2004.08.013>.
- [49] Gomez-Jeria, J. S., An Empirical Way to Correct Some Drawbacks of Mulliken Population Analysis. *J. Chil. Chem. Soc.* **2009**, *54*(4), 482-485. <http://dx.doi.org/10.4067/S0717-97072009000400036>.